Title: Degradation mechanisms of perovskite solar cells under vacuum and one atmosphere of nitrogen

Authors: Renjun Guo[1,10], Dan Han[2,10], Wei Chen[1,3,10], Linjie Dai[4], Kangyu Ji[4], Qiu Xiong[5], Saisai Li[6], Lennart K. Reb[1], Manuel A. Scheel[1], Shambhavi Pratap[1], Nian Li[1], Shanshan Yin[1], Tianxiao Xiao[1], Suzhe Liang[1], Anna Lena Oechsle[1], Christian L. Weindl[1], Matthias Schwartzkopf[7], Hubert Ebert[2], Peng Gao[5], Kai Wang[3], Mingjian Yuan[6], Neil C. Greenham[4], Samuel D. Stranks[4], Stephan V. Roth[7,8], Richard H. Friend[4], Peter Müller-Buschbaum[1,9*]

Affiliations:

[1]Lehrstuhl für Funktionelle Materialien, Physik-Department, Technische Universität München, 85748 Garching, Germany

[2]Department Chemie, Ludwig-Maximilians-Universität München, 81377 München, Germany

[3]Department of Electrical and Electronic Engineering, Southern University of Science and Technology, 518055 Shenzhen, China

[4]Cavendish Laboratory, University of Cambridge, CB3 0HE Cambridge, UK

[5]Fujian Institute of Research on the Structure of Matter, 350002 Chinese Academy of Sciences, Fuzhou, China

[6]Department of Chemistry, Nankai University, 300071 Tianjin, China

[7]Deutsches Elektronen-Synchrotron (DESY), 22607 Hamburg, Germany

[8]Department of Fiber and Polymer Technology, KTH Royal Institute of Technology, 10044 Stockholm, Sweden

[9]Heinz Maier-Leibnitz-Zentrum, Technische Universität München, 85748 Garching, Germany

[10]These authors contributed equally: Renjun Guo, Dan Han, Wei Chen

*Correspondence to: muellerb@ph.tum.de

Abstract: Extensive studies have focused on improving the operational stability of perovskite solar cells but few surveyed the fundamental degradation mechanisms. One aspect overlooked in earlier works is the effect of the atmosphere on the device performance during operation. Here, we investigate the degradation mechanisms of perovskite solar cells operated under vacuum and a nitrogen atmosphere using synchrotron radiation-based *operando* grazing-incidence X-ray scattering methods. Unlike what was seen in previous reports, we find that light-induced phase segregation, lattice shrinkage, and morphology deformation occur under vacuum. Under nitrogen, only lattice shrinkage appears during the operation of solar cells resulting in a better device stability. The different behavior in nitrogen is attributed a larger energy barrier for lattice distortion and phase segregation. Finally, we find that the migration of excessive PbI_2 to the interface between the perovskite and the hole transport layer degrade the performance of devices either under vacuum or nitrogen.

Solution-processed hybrid halide perovskite materials have attracted strong interest for next-generation thin-film photovoltaic applications due to their high power conversion efficiency (PCE) and low fabrication costs compared to silicon photovoltaics[1]. With solvent engineering, compositional tuning, and surface passivation[2–4], the highest PCE of perovskite solar cells (PSCs) has reached 25.5 %[5]. Moreover, possibility of fabricating PSCs on flexible substrates opens up promising manufacturing routes, and novel application fields are explored, such as lightweight photovoltaic devices for space applications. Previous studies showed that PSCs were successfully operated in space with low vacuum conditions such as on a high-altitude balloon and a suborbital rocket[6–8]. Although these pioneers confirmed the possibility of operating PSCs in space, the operational stability of PSCs is unknown under such conditions. In terrestrial studies, vacuum conditions play a major role in the performance loss of PSCs during operation. Thus, although there is such a rapid increase in the PCE, very significant challenges remain. More research is required to increase the stability of the materials and the longevity of the devices, as long-term operational stability remains the main challenge for real-world applications of hybrid halide perovskite materials. Therefore, investigating the performance degradation mechanism of PSCs under different atmospheric conditions is one key approach to further improving the long-term operational stability of PSCs[9].

Exposure to above-bandgap illumination can cause a loss of phase and structure stability for perovskite materials. For instance, phase segregation introduced by lattice distortion, halide migration, and crystalline reorganization can cause an open-circuit voltage penalty arising from halide segregation[10]. In addition, several studies have indicated that a lattice distortion under illumination originates from light excitation or thermal expansion[11–13]. Although the above studies discuss light-induced phase and lattice behaviors, all experiments were executed under different atmospheres, based on different perovskite systems and architectures. Due to these reasons, the results of these studies are inadequate to give a

comprehensive understanding of the mechanisms of light-induced lattice effects by themselves and are in need of complementary data. There is no doubt that different macroscopic operation conditions (especially different atmospheres) can profoundly influence the microscopic behavior of PSCs[14]. To this end, Khenkin and co-workers proposed experimental procedures based on the International Summit on Organic Photovoltaic Stability (ISOS) protocols[15]. Although the ISOS protocol suggests using a vacuum or inert nitrogen atmosphere as the standard, the effects of those two conditions on the morphology and optoelectronic properties of PSCs have not been investigated systematically yet. To direct scientific progress towards commercial applications, the degradation mechanism of PSCs, specifically including the microscopic and macroscopic behavior of PSCs needs to be fully understood under vacuum and in a nitrogen atmosphere, respectively.

Here, we report that mixed-cation mixed-halide lead perovskite $(MAPbBr_3)_{0.17}(FAPbI_3)_{0.83}$ (MAFA) PSCs experience a significant lattice shrinkage, a phase segregation into a $FAPbI_3$ phase as the minority phase, and a large amount of $(MAPbBr_3)_{0.17+x}(FAPbI_3)_{0.83-x}$ as the majority phase for the perovskite layer under standard one-sun illumination (AM1.5 G) in vacuum. The intrinsically different crystallite orientations of the two perovskite phases offer a pathway for phase segregation. Meanwhile, the phase segregation of the perovskite materials introduces a coherent phase boundary to decrease the film strain. In contrast, continuous operation in nitrogen under the same illumination intensity has only a minor effect on the lattice dynamics of the perovskite materials. Thus, atmospheres affect the morphology deterioration of the perovskite layer. Calculations through density functional theory (DFT) reveal that the thermodynamic driving force for lattice distortion and phase segregation of the perovskite material is highly atmosphere-dependent. Experimental results and device simulations jointly prove the relationship between physical changes and

device performance. We highlight the significant effects of atmospheres on the degradation pathways of devices, even with applied the ISOS protocol.

Device performance and material characterization

We fabricate planar MAFA PSCs *via* the anti-solvent method, as previously reported[16]. Fig. 1a presents the device architecture of the studied PSCs. The PCE of the champion device equals the certified record of MAFA perovskite solar cells (Fig. 1b)[17]. Fig. 1c shows the related histogram of the PCE data for 36 devices. The narrow steady-state photoluminescence spectrum and the sharp edge in the absorbance spectrum for MAFA perovskite films suggest uniformity and phase purity (Supplementary Fig. 1a)[18]. Top view scanning electron microscopy (SEM) and cross-section SEM images show smooth perovskite films, indicating the formation of condensed grains without pin-holes (Supplementary Fig. 1b and 1c). X-ray diffraction data (Supplementary Fig. 2a and 2b) show Bragg reflexes from δ-$FAPbI_3$ and PbI_2 phases. The existence of these phases in perovskite films was reported to boost the PCE of perovskite solar cells[19,20]; however, an excessive amount of PbI_2 leads to a poor device performance[21]. These material properties and device efficiencies are of critical importance for this state-of-the-art research about degradation.

Structural changes during operation of the devices

Through the *operando* grazing-incidence wide-angle X-ray scattering (GIWAXS) studies on the MAFA PSCs via the ISOS-L-1I protocol (with continuous voltage-bias scan and illumination in inert atmospheres), we find lattice shrinkages to different extents under different atmospheres. Pictures of the *operando* set-up are shown in Fig. 1d and Supplementary Fig. 3. The detailed experimental conditions and data treatment are listed in the Methods section and

Supplementary Note.1. The scattering depth for the MAFA perovskite is 660 nm at the used incident angle of 0.4°, which ensures that we measure the statistical bulk information of the PSCs (Supplementary Fig. 6 and Supplementary Note 2).

Under vacuum, the time evolution of 2D GIWAXS data demonstrates a significant lattice shrinkage and phase segregation into the minority phase $FAPbI_3$ and the majority phase $(MAPbBr_3)_{0.17+x}(FAPbI_3)_{0.83-x}$ during the operation of the PSCs (Fig. 2a and 2c). The (100) Bragg peak position of the MAFA perovskite experiences a dramatic shift after 45 min of illumination (increasing from 0.998 $Å^{-1}$ to 1.018 $Å^{-1}$), proving a dramatic decrease of the interplane spacing of the crystal. This initial shift of the (100) Bragg peak position is followed by a slight back shift (decreasing from 1.018 $Å^{-1}$ to 1.010 $Å^{-1}$), coinciding with the phase segregation as seen in the (210) Bragg peak. In contrast, the time evolution of the line profiles, azimuthally integrated from the 2D GIWAXS scattering data, indicates that the MAFA perovskite undergoes only a slight lattice shrinkage in nitrogen (Fig. 2b). Since different Bragg peaks reflect different lattice spacings in the materials, we assign the Bragg peak (hkl) of the cubic structure with the following equation:

$$d_{hkl} = a\sqrt{h^2 + k^2 + l^2} \quad (1)$$

where a, d_{hkl}, (h,k,l) refers to the lattice parameters, interplane spacing, and Miller indices, respectively. According to the cubic model, the degree of lattice shrinkage extracted from the (110) and (111) Bragg peaks is different compared with the measured data of the (100) Bragg peak for the whole illumination period (Fig. 2d and Supplementary Fig. 7a and 7b). Therefore, the lattice shrinkage of the MAFA perovskite is non-uniform under the operation in both atmospheres because lattice constants are different in different lattice planes. In addition, Supplementary Fig. 7c shows that the emergence of Bragg peaks around 1.6 $Å^{-1}$ indicates the formation of the tetragonal perovskite phase caused by a non-uniform lattice shrinkage, which was also found by a previous study due to a composition change[22].

We further use the Williamson-Hall analysis for azimuthally integrated line profiles to track the film strain evolution under both atmospheres (Supplementary Note 3,4 and Supplementary Fig. 8). During the operation of PSCs under vacuum, the strain of the MAFA perovskite layer increases first, then decreases slightly after the phase segregation into a minor phase $FAPbI_3$, and a major phase $(MAPbBr_3)_{0.17+x}(FAPbI_3)_{0.83-x}$ appears. In contrast, the film strain releases slightly under operation in a nitrogen atmosphere, and is below the film strain found in vacuum. In addition, the (210) Bragg peak of MAFA splits up with the increase of the operation time under vacuum, indicating a phase segregation and the formation of the new components MAFA and $FAPbI_3$ as a result of 45-min operation under vacuum (Fig. 2e)[23]. The release of the film strain happens with phase segregation at the (210) plane, indicating that this plane is the habit plane due to its low film strain[24]. We calculate the misfit of the separated (210) Bragg peaks at 120 min by using equation (2):

$$\delta = \frac{2(d_{FAPbI_3} - d_{MAFA})}{d_{FAPbI_3} + d_{MAFA}} \quad (2)$$

We obtain $\delta = 0.022$ (<0.05), which is the certification of the formation of a coherent phase boundary[25]. Coherent phase boundaries have a lower energy and can enhance the strength and phase stability of the MAFA perovskite layer[26]. Although condensed grains are observed by SEM imaging, a local crystal misorientation may exist and produce a local structural strain. Thus, a potential phase segregation would be driven by such local crystal misorientations[27]. Such a scenario is also confirmed by Supplementary Fig. 9a, which shows that $FAPbI_3$ crystallite orientations already exists before the phase segregation. This finding indicates that the crystallite orientations of MAFA perovskite films occurs already during the fabrication process, which will drive the phase segregation under operation. The broadening of the crystallite orientations seen in Fig. 2f and Supplementary Fig. 9b-9e with increasing operation

time indicates that the orientations of both, the MAFA and $FAPbI_3$ become more disordered after continuous operation.

The results from measurements on top of the gold top contact also confirm that the structural evolution is not affected whether the monitoring positions are on the electrode or just beside the electrode (Supplementary Fig. 4a, 4b, 4c and 4f). When PSCs operate under the ISOS-L-2I protocol with an increased temperature (55 ^{o}C) in nitrogen, the perovskite lattice shows a slightly stronger lattice shrinkage tendency (Supplementary Fig. 4d and 4g). The Supplementary Fig. 4e and 4h confirm that PbI_2 and δ-$FAPbI_3$ phases are less likely to affect the lattice distortion because PSCs with the pure-phase component $Cs_{10}FA_{90}PbI_3$ also experience a lattice shrinkage under operational conditions (ISOS-L-1I). According to the above observations, we claim that the mixed cation lead mixed halide perovskites experience lattice shrinkages and phase segregation during the operation of the PSCs under vacuum. A nitrogen atmosphere with a standard atmospheric pressure serves as one useful condition to minimize the effects of lattice shrinkages and phase segregation during the operation of the PSCs.

Morphology changes under the operation of devices

We use grazing-incidence small-angle X-ray scattering (GISAXS) to investigate the morphology evolution of PSCs under operation in different atmospheres (Fig. 3a and Fig.3d). To quantify our results from the 2D GISAXS data, we survey the temporal evolution of the intensities in the horizontal line cuts and model these data with form and structure factors (Supplementary Fig. 10). The superposition of Gaussian distributed form factors used for modeling the GISAXS data relates to the crystal size distribution because the intensity scales linearly with the number of crystals of a specific size (Supplementary Note 5 and 6). Fig. 3b and 3c show that the number of small crystals increases during operation under vacuum. Our

results show that crystals with diameters lower than 40 nm break into smaller crystals. These small crystals act as pinholes in the PSCs[28]. The increasing number of crystals also introduces an increasing number of grain boundaries. This phenomenon is known as grain boundary strengthening, which can, in turn, increase the strength of the MAFA perovskite film under operation in vacuum[29]. It can stop a further degradation of the MAFA perovskite film. In contrast, we do not observe a similar phenomenon in nitrogen (Fig. 3e).

Eperon et al. showed the existence of porosity in the perovskite film using a gas pycnometer, and this porosity could offer a physical pathway for the origin of the nitrogen adsorption process[30]. To confirm this, we measure the adsorption behavior of the MAFA perovskite material in nitrogen *via* the Brunauer-Emmett-Teller method (Supplementary Fig. 11). Indeed, the MAFA perovskite can adsorb more nitrogen as the pressure of nitrogen increases. The perovskite sample exhibits a type III isotherm, which indicates the formation of a nitrogen molecule multilayer around the perovskite layer during the operation of PSCs under nitrogen[31]. For the PSCs used in this study, most of their module area is not covered by electrodes, which means that the majority of spiro-OMeTAD layer can directly contact the atmosphere. The loose space structure of spiro-OMeTAD offers pathways, which allows for the diffusion of nitrogen molecules into the active layer underneath (Fig. 3f). Hence, we suggest that a nitrogen atmosphere under standard pressure helps to stabilize the morphology of the perovskite film during operation. Meanwhile, we highlight the importance of large crystals for enhancing the stability of perovskite materials.

Mechanisms of atmosphere-dependent operational stability

To investigate the intrinsic driving force for phase segregation and lattice shrinkage, we combine the aforementioned structure and morphology evolution with thermodynamic kinetics to provide an interpretation. For the calculations, we focus on the $(MAPbBr_3)_{0.2}(FAPbI_3)_{0.8}$

component. We first use the Gibbs free energy to evaluate the effect of pressure on the free energies of perovskite components, in contrast to a previous report, which applied a GPa-level pressure to suppress the phase segregation of mixed halide perovskites under illumination[32]. Atmospheric pressure can only decrease the Gibbs free energy by 1.29×10^{-7} eV due to the use of a relatively low pressure (1.01×10^5 Pa) in our study. Hence, in our study, the increased pressure from the nitrogen atmosphere largely does not affect the free energy and cannot be the reason for the suppression of phase segregation. Thus, we use Helmholtz free energy to calculate the free energy of the mixing perovskite phases below. Previous studies have efficiently proven that the lattice shrinkage can increase the activation energy barrier to suppress phase segregation due to the decrease of ion migrations[33]. However, perovskite films under illumination in vacuum can increase the doping concentration for all hybrid perovskite materials due to the decomposition induced by volatile species or the gas desorption induced defects in the crystal structures[34]. Simultaneously, the relative permittivity of perovskite materials can change when illumination or pressure are applied[35,36]. Thus, we recalculate the activation energy of the phase segregation under operation conditions in different atmospheres by means of the method used in references to show the potential for phase segregation[33].

We find negative activation energies of the MAFA perovskite under operation in vacuum, indicating that the phase segregation could occur spontaneously at room temperature (Fig. 4a). In contrast, a positive activation energy in the case of operation in nitrogen indicates a much larger energy barrier for the phase segregation, significantly preventing phase segregation. Fig. 4b shows that perovskites with different components display different thermodynamic phase stabilities. When the free energy of the mixing perovskite phase (ΔF_{mix}) is larger than 0, phase segregation is energetically favorable for the corresponding secondary phases. Additionally, the phase segregation energy (ΔF_{sep}) for different concentrations x for $(MAPbBr_3)_x(FAPbI_3)_{1-x}$ illustrates a concave upward curvature of ΔF_{mix} ranging from $x = 0$ to $x = 0.2$, indicating a

thermodynamically stable mixed phase at room temperature. The concave downward curvature of ΔF_{mix} from $x > 0.2$ refers to metastable ($\Delta F_{mix}<0$) and unstable states ($\Delta F_{mix}>0$) for the MAFA perovskite. However, ΔF_{mix} will increase if we take the influence of photo-excited carriers (n = 0-0.26/f.u.) into consideration, and this results in a thermodynamic driving force for the phase segregation of the perovskite film[11]. This observation is also consistent with previous reports, which pointed out that perovskite materials tend to be phase-separated as Br content increases[23,37].

Next, we link the thermodynamic kinetics with the structure and morphology evolution process. Fig. 4c shows the lattice volume as a function of the composition ratio of $MAPbBr_3$ and $FAPbI_3$. We calculate it by using the crystallographic information file (Supplementary Table. 1-4). Corresponding changes of MAFA perovskite lattice volumes as a function of operation time in different atmospheres are also taken into consideration. Under vacuum, the operation of PSCs demonstrates a strong lattice shrinkage to suppress the trend of spontaneous phase segregation at room temperature (Fig. 4a and Supplementary Fig. 7a). After a 45-min operation in vacuum, the lattice volume reaches about 235 $Å^3$, which is the expected value for the lattice volume of the component $(MAPbBr_3)_{0.45}(FAPbI_3)_{0.55}$. Hence, the film strain increases dramatically due to such a lattice shrinkage. The dramatically compressed lattices perturb the balance between the film strain and the phase stability. The intrinsically different crystallite orientations for the MAFA phase and $FAPbI_3$ offer a starting point for phase segregation. To maintain the metastability of the $(MAPbBr_3)_{0.17}(FAPbI_3)_{0.83}$ PSCs during operation in vacuum, $FAPbI_3$ crystals precipitate from the (210) habit plane, thereby releasing the film strain (Fig. 2e and Supplementary Fig. 8c). This process also forms a coherent phase boundary, which could increase the strength of the perovskite film and suppress further phase segregation. Moreover, small size crystals break to maintain the low energy of the whole system, and thus introduce a grain-boundary strengthening. Finally, the lattice volume reaches

approximately 240 $Å^3$, which is the expected value for the component $(MAPbBr_3)_{0.28}(FAPbI_3)_{0.72}$. This component has a negative value of ΔF_{mix} even under strong illumination, indicating a metastable mixed perovskite phase state.

We speculate that there are four causes for the observed phase segregation, severe lattice shrinkage, and broken crystals under vacuum, as illustrated in the schemes in Fig. 3c and Fig. 4d: 1) a significant mismatch between the compressed lattice volume and the real components of the film, 2) intrinsically different crystallite orientations of the MAFA and $FAPbI_3$, 3) the need to decrease the film strain introduced by phase segregation and the formation of the coherent phase boundary and 4) the demand to strengthen the perovskite film to suppress further deformation through the increase of grain boundaries due to broken crystals.

Physical adsorption of gas molecules can decrease the free energy *via* an exothermic process[38]. Thus, we speculate that the physical adsorption of nitrogen could play an important role in reducing the film strain and maintaining the lattice and phase stability, which is also related to a larger activation energy barrier for phase segregation as discussed above. This observation is similar to the study of Alberti *et al.*, who showed that a nitrogen-assisted process played an important role in the lattice recovery during the annealing process, and that long-term operational stability can be improved by device encapsulation inside a pure nitrogen atmosphere[39].

Different degradation pathways and relative performance

We examine the temporal device performance of MAFA PSCs under operation conditions in the two different atmospheres. Devices operated in nitrogen show a better stability in terms of open-circuit voltage (V_{OC}), fill factor (FF), and PCE, compared with those operating under vacuum. Fig. 5a shows a decrease of 20 % for the V_{OC} and 10 % for the FF under vacuum (normalized from 6 devices, Supplementary Fig. 12a and 12b show the

exemplary J-V evolution from one of these devices). In contrast, PSCs show only a 10 % decrease of the V_{OC} in a nitrogen atmosphere (Fig. 5b). To identify the mechanisms for these losses, we measure transient absorption (TA) spectra for a MAFA perovskite film within 120 minutes of exposure to a white-light spectrum under vacuum. Fig. 5c shows that there is no peak shift for the perovskite film with white light soaking under a high-vacuum condition, indicating that the decrease of V_{OC} is not due to the worse band alignment[40]. Because the power of a white-light lamp is lower than that of the AM1.5 G spectrum, we execute 480-min illumination to obtain a comparable dose of illumination. Detailed analysis (Supplementary Fig. 13) suggests that illumination is less likely to change the non-radiative relaxation of higher electronic states, vibrational relaxations, and radiative relaxations of the perovskite even after 480-min illumination.

To further confirm this finding, we measure the photovoltaic external quantum efficiencies (EQEs) for the fresh PSCs and the same PSCs after the degradation process under vacuum. Indeed, Fig. 5d shows that the feature of $FAPbI_3$, as the minority phase, appears after phase segregation. This could be due to an outgassing process of MA molecules from the perovskite layer when the PSCs are operated under vacuum[41]. Hence, phase segregation occurs only when PSCs are operated under vacuum, agreeing well with the GIWAXS study discussed above. This minority phase leads to an increasing charge carrier density due to energetic confinement within a small fraction of the total film volume. All charge carriers tend to funnel into the $FAPbI_3$ having the lowest bandgap. This increased charge carrier density could increase the radiative recombination, given that the bimolecular radiative recombination process is much stronger than the monomolecular non-radiative recombination[10]. The same study suggested that the V_{OC} loss is pinned by the increasing amount of a low bandgap iodide-rich phase. We execute the device simulation *via* SCAPS-1D based on the 'drift-diffusion' model to simulate the effects on devices by increasing the radiative recombination coefficient

of the perovskite materials[42]. Even if the radiative recombination coefficient of the MAFA perovskite increases from 3.16×10^{-12} to 3.16×10^{-6} in the simulation for the perovskite layer, there is only a voltage penalty of 26 mV (Supplementary Fig. 12c and 12f). Thus, the larger voltage loss observed in vacuum conditions cannot result only from phase segregation.

Given that phase segregation of PSCs does not influence the device performance strongly, we predict that there must be additional changes at interfaces affecting the final device performance significantly. A previous study using advanced *in situ* transmission electron microscopy revealed that the voltage-bias scan for PSCs could cause the formation of PbI_2 nanoparticles between the perovskite and the spiro-OMeTAD interface[43]. We confirm this phenomenon *via* an XPS study (Fig. 5e). From a detailed quantitative analysis (see Supplementary Note 7), we find that the I/Pb ratio decreases from 3.11 to 2.71 after a continuous voltage-bias scan for 30 min. The decrease of the I/Pb ratio confirms that PbI_2 migrates into the interface between the perovskite film and spiro-OMeTAD.

We also investigate the effect of existing PbI_2 between the perovskite and the hole-transport layer using a simulation of the 'drift-diffusion' model. We find a voltage loss of 90 mV after inserting a PbI_2 layer between the perovskite and the hole-transport layer, showing that the excess PbI_2 at the interface reduces the V_{OC} dramatically (Supplementary Fig. 12d). In addition, a control experiment for PSCs without excess PbI_2 under operation in a different atmospheric condition is executed. The drop of V_{OC} for PSCs is significantly suppressed after 120 min illumination in both, vacuum and nitrogen conditions (Supplementary Fig. 14). Hence, we confirm that, under voltage-bias conditions, excess PbI_2 migrates to the interface between the perovskite and the spiro-OMeTAD layer irrespective of the type of atmosphere, thereby degrading the V_{OC} of the devices. The existence of PbI_2 changes the heterojunction type for PSCs from the staggering gap (type II) to the straddling gap (type I) because of the larger bandgap of PbI_2 (Fig. 5f). This change forms a worse band alignment for transporting holes.

Furthermore, the GISAXS data show that small crystals break up during operation under vacuum, which can create pinholes. This results in shunting pathways, dramatically decreasing the shunt resistance of the devices[44]. From the 'drift-diffusion' simulation, we find that a decrease of the shunt resistance results in a decrease of the FF and V_{OC} of the devices decreases (Supplementary Fig. 12e). This finding supports our results of a stronger degradation during operation under vacuum. Overall, the PbI_2 migration is one mechanism, which causes voltage loss and occurs for PSCs in both atmospheres. The segregation of the minority phase and the formation of small crystals from larger crystals (~40 nm) cause an additional voltage loss and a severe FF loss during operation under vacuum.

Conclusion

We discover the kinetics between structural changes and phase segregation, and explain them in detail regarding thermodynamic theory. We also reveal the atmosphere-dependent degradation mechanisms for PSCs under different operation conditions. Operating PSCs under vacuum causes both, a large degree of lattice shrinkage and a spontaneous process for phase segregation of the mixed cation lead mixed halide PSCs. Importantly, these effects are mitigated in nitrogen. Therefore, we suggest using a nitrogen atmosphere with an ambient pressure as a standard atmosphere for guiding scientific research and industrial development in the perovskite field. Furthermore, these new findings provide a constructive way to improve the long-term operational stability of this emerging photovoltaic technology *via* nitrogen encapsulation or the lattice fine-modification of perovskite materials.

Methods

Precursor preparation. The tin (IV) oxide 15% in H_2O colloidal dispersion (Alfa Aesar, 44592) was diluted with deionized water with a volume ratio of 1:4, and was shaken for 2 hours at room temperature. The MAFA perovskite solution was prepared by first mixing the powders methylammonium bromide (22.4 mg, Greatcellsolar, MS301000), lead bromide (73.4 mg, Alfa Aesar, A19406), formamidinium iodide (172 mg, Greatcellsolar, MS150000) and lead iodide (485 mg, Sigma-Aldrich, 554359-5G). Then, 640 µL DMF (Acros, 348435000) and 160 µL DMSO (Acros, 348441000) were added into the mixed powders. The obtained mixture was dissolved and stirred at 70 ºC for 30 minutes, followed by stirring at room temperature for 30 minutes. The solution was used up within in 2 hours after preparation. The $Cs_{10}FA_{90}PbI_3$ perovskite solution was mixed by Caesium iodide (31.2 mg, abcr GmbH, AB207757), formamidinium iodide (192.6 mg), and PbI_2 (576.3 mg) in 800 µL DMF and 200 µL DMSO. The obtained solution was stirred at room temperature for 2 hours. The spiro-OMeTAD solution was mixed of spiro-OMeTAD (72.3 mg, Sigma-Aldrich, 902500), 1 mL chlorobenzene (Acros, 443001000), 17.5 µL Li-TFSI (520 mg/mL (Sigma-Aldrich, 544094) in acetonitrile (Sigma-Aldrich, 2710004)), and 28.8 µL 4-tert-butylpyridine (Sigma-Aldrich, 142379).

Device fabrication. We fabricated perovskite solar cells as described in previous publications [45,46]. The patterned indium doped tin oxide (ITO from Lumtec, LT-G001) substrates (25 mm × 25 mm) were immersed and washed in diluted Hellmanex® III (2:98) solution (Sigma-Aldrich, Z805939-1EA), deionized water, acetone, isopropanol and ethanol in the ultra-sonication bath for 10 minutes each. Then the substrates were dried at 80 ºC in the oven. Before spin-coating the diluted tin oxide solutions, the substrates were treated by oxygen plasma for 10 min with 168 W. The tin oxide solution was spin-coated at 3000 r.p.m. (1000 r.p.m./s) for 30 s, followed

by annealing at 150 ºC for 30 minutes. After the substrates cooled down, the substrates were transferred into a nitrogen-filled glove box. The perovskite precursor was spin-coated on ITO/SnO_2 substrates at 6000 r.p.m. (800 r.p.m./s) for 30 s, and we rapidly added 70 µL chlorobenzene into the center of substrates under a vertical angle at 5 s before ending, followed by 40-60 minutes annealing at 100 ºC. For the $Cs_{10}FA_{90}PbI_3$ component, we slowly added 120 µL chlorobenzene into the center of substrates under a vertical angle at 15 s before ending, followed by 15 minutes annealing at 150 ºC. When the substrates were cooled down, we dynamically spin-coated spiro-OMeTAD solution on ITO/SnO_2/perovskite substrates at 4000 r.p.m for 20 s. Then, all the substrates were stored in a dark-desiccator with silica gel (< 10 % rel. humidity) for 24 hours to increase the conductivity of the spiro-OMeTAD layer. Finally, an 80 nm thick Au layer was evaporated on the spiro-OMeTAD layer with 2 nm (0.2 Å/s) and 78 nm (1.2 Å/s) at a pressure of 10^{-5} bar. The devices were kept in the desiccator and measured regularly until the efficiency reached stable values.

Solar cell characterization. The current density-voltage (J-V) data were recorded using a Keithley 2611B source meter under the illumination of a solar simulator (class ABA) with a light intensity of 100 mW cm^{-2}, which was calibrated with a reference solar cell (Fraunhofer ISE019-2015). The solar cells were measured with a scanning speed of 50 mVs^{-1} (voltage step of 10 mV and integration time of 100 ms). There were 6 (or 8) gold top electrodes with a dimension of 2.5×10.0 mm (or 3.5×10.0 mm) for each substrate on a substrate with a size of 25×25 mm. The active area was controlled by a metal shadow mask (0.12 or 0.19 cm^2) to avoid overestimation of the photocurrent.

The external quantum efficiencies (EQEs) were measured by Oriel® Quantum Efficiency Measurement Kit from the Newport company. The light source spectrum response was

calibrated by the silicon detector. The measurements were performed using the Oriel Instruments QEPVSI-b system with a Xenon arc lamp (Newport 300 W, 66902) chopped at 30 Hz and a monochromatic instrument (Newport Cornerstone 260). The EQE was measured and normalized in the wavelength range of 350 to 900 nm.

Material characterization. The surface morphology was probed with a field-emission scanning electron microscopy (SEM, Zeiss NVision 40) with an acceleration voltage of 5 kV at a working distance of 3.5 mm. Photoluminescence spectroscopy was performed with a Picoquant Fluotime 300 spectrofluorometer, using an excitation wavelength of 370 nm. Ultraviolet-visible (UV–vis) absorption spectra were measured using a Lambda 35 (PerkinElmer).

***Operando* synchrotron radiation-based grazing incidence small/wide-angle x-ray scattering.** The *operando* experiments were executed at beamline P03 at Deutsches Elektronen-Synchrotron (DESY, Hamburg) during two separate beamtimes to ensure reproducibility[47,48]. The wavelength of the monochromatic X-ray beam was set to 11.65 keV and 11.70 keV to avoid the absorption edge of lead (around 13 keV) and thus minimize X-ray radiation damage. 2D GIWAXS data were collected at an incident angle of 0.4° with Pilatus 300K (Dectris Ltd., pixel size 172 µm) and LAMBDA 4.5M (X-Spectrum GmbH, pixel size 55 µm) detectors. 2D GISAXS data were collected at the same incident angle (0.4°) with Pilatus 1M and Pilatus 300K detectors. The parameters of beam center and the sample-to-detector distance (SDD) of GISAXS detector images were calibrated *via* fits of the patterns of LaB_6 powders using the DPDAK package[49]. The parameters of beam center and the sample-to-detector distance of GIWAXS detector images were calibrated *via* fits of the patterns of CeO_2 powders using the DPDAK package. The GISAXS detector images were further treated *via*

DPDAK package based on Python 2.7. The reciprocal q-space GIWAXS scattering images, the line cuts and azimuthal integrations of the scattering data were obtained with the GIXSGUI MATLAB plug-in[50]. To calibrate the intensity of different scattering images, we normalized it to the ionization energy of the incident X-ray beam for each frame.

Conditions of the synchrotron radiation-based *operando* grazing-incidence X-ray scattering method. The *operando* grazing-incidence wide-angle X-ray scattering (GIWAXS) studies on the MAFA PSCs were done *via* the ISOS-L-1I protocol (with continuous voltage-bias scan and illumination) to unify the experimental assessment. ISOS-L-1I stands for the intrinsic photo-stability at room temperature (similar to ISOS-L-1 except that the atmosphere is inert). The pressures were kept at 5×10^{-1} Pa for the vacuum condition and 1.01×10^{5} Pa for a pure nitrogen atmosphere, respectively. The entire *operando* measurement chamber was stabilized at 25.0 ± 0.7 ˚C with a water-cooling system, which was monitored by an infrared thermometer.

Gas adsorption measurement. Perovskite single crystals were synthesized by the method offered in previous work[51]. In short, methylammonium bromide (22.4 mg), lead bromide (73.4 mg), formamidinium iodide (172 mg) and lead iodide (485 mg) were dissolved in 1 mL gamma butyrolacton solution at a hotplate with 65 ºC in a nitrogen glovebox until the solution became clear. This precursor solution was annealed to 100 ºC to grow single crystal seeds. A new precursor solution was used after that to get large crystals. The single crystal was grinded to get perovskite powder. Nitrogen adsorption measurements were performed using a Micromeritics ASAP 2420 instrument. Before the adsorption measurements, 0.68 g perovskite

455 powder were out-gassed at 85 °C for 10 hours in vacuum. The measurement was carried out in
456 a 77 K liquid N_2 bath.
457
458 **Computational Methods.** The Gibbs free energy of the mixed cation and mixed halide hybrid
459 perovskite $(MAPbBr_3)_x(FAPbI_3)_{1-x}$ was evaluated *via*

460 $$\Delta G(x) = \Delta U(x) - T\Delta S(x) + P\Delta V \quad (3)$$

461 where the $\Delta U(x)$ and $\Delta S(x)$ are mixing energy and entropy of perovskite phases. T, P
462 and ΔV is the temperature, pressure and the change of the volume of the system. The mixing
463 energy $\Delta U(x)$ is defined as:

464 $$\Delta U(x) = U_x - (1-x)U_{FAPbI_3} - xU_{MAPbBr_3} \quad (4)$$

465 where U_x, U_{FAPbI_3} and U_{MAPbBr_3} are the calculated DFT total energies per formula unit of
466 $(MAPbBr_3)_x(FAPbI_3)_{1-x}$ and the pure $FAPbI_3$ and $MAPbBr_3$, respectively.
467 The mixing entropy was

468 $$\Delta S(x) = -k_B[x\ln x + (1-x)\ln(1-x)] \quad (5)$$

469 in which k_B is the Boltzmann constant.
470 Without the $P\Delta V$ term, the expression of free energy is

471 $$\Delta F(x) = \Delta U(x) - T\Delta S(x) \quad (6)$$

472 where $\Delta U(x)$ and $\Delta S(x)$ follow from the Equations (9) and (10).
473 The free energy upon illumination was estimated following the method mentioned in Ref [11,52].
474 We assumed that when $(MAPbBr_3)_x(FAPbI_3)_{1-x}$ was under illumination, pairs of photo-

generated charge carriers were generated uniformly in the material at a density (per formula unit) *n*, then the free energy becomes

$$\Delta U_x^* = \Delta U_x + nE_g(x) \quad (7)$$

for the unmixed state $(1-x)$FAPbI$_3$ + xMAPbBr$_3$, it was assumed that all charge carriers funnel into the FAPbI$_3$, so the total energy of photoexcited FAPbI$_3$ becomes

$$\Delta U_{FA}^* = \Delta U_{FA} + n\frac{1}{1-x}E_g^{FA} \quad (8)$$

using Eqs. (10) and (11) in Eq. (7), with U_x and U_{FA} substituted by U_x^* and U_{FA}^*. We obtained

$$\Delta U^*(x) = \Delta U(x) + n\left(E_g(x) - E_g^{FA}\right) \quad (9)$$

The free energy of mixing of (MAPbBr$_3$)$_x$(FAPbI$_3$)$_{1-x}$ under the photo illumination becomes

$$\Delta F^*(x) = \Delta F(x) + n\left(E_g(x) - E_g^{FA}\right) \quad (10)$$

The slope of ΔF_{mix} referred to the phase stability of materials:

$$\Delta F_{sep} = \frac{\sigma^2 \Delta F_{mix}}{\sigma x^2} \quad (11)$$

which indicated that mixed phases maintained stable when the curvature was convex ($0<x<0.2$ in our case), while mixed phases started to separate when the curvature was concave ($0.2<x<1$ in our case) [53].

The DFT calculations were performed using the Vienna *Ab initio* Simulation Package (VASP) code[54]. A revised Perdew-Burke-Ernzerhof generalized gradient approximation (GGA) functional (PBEsol) was used for the exchange-correlation functional[55]. The supercell method was employed for the simulation of the phase (MAPbBr$_3$)$_x$(FAPbI$_3$)$_{1-x}$ (x = 0.2, 0.3, 0.5, 0.8). Accordingly, 1 x 5 x 1, 2 x 2 x 1, 2 x 5 x 1 supercells were constructed for x=0.2 (0.8), 0.5, 0.7 based on a 12-atom cubic unit cell of MAPbBr$_3$. Then we substituted MA cations by FA cations

and Br anions by I anions at different concentrations. For these 3 and 4 possible configurations were considered for $(MAPbBr_3)_x(FAPbI_3)_{1-x}$ with x=0.2 (0.8), 0.5, 0.7, respectively. The total energy of the configurations belonging to the same concentration was averaged to obtain the total energy for the phases (U_x). A cubic-phase crystal structure was utilized for the calculations of the pure compounds $MAPbBr_3$ and $FAPbI_3$, which corresponds to x=0 and 1 in $(MAPbBr_3)_x(FAPbI_3)_{1-x}$. A plane-wave basis set with a cutoff of 500 eV was used and the convergence criteria for the total energy was set to 10^{-5} eV. All lattice vectors and atomic positions were fully relaxed until the Hellman-Feynman forces on each atom were less than 0.01 eV $Å^{-1}$. A Monkhorst-Pack k-point mesh with a grid spacing of ~$2\pi\times0.02$ $Å^{-1}$ was used for the Brillouin zone integration. Spin-orbit coupling (SOC) was not taken into account for all calculations since preceding studies noted that the bandgap calculated using GGA (PBE or PBEsol) without SOC showed reasonable agreement with the experimental bandgap due to a cancellation of errors[56–58].

The activation energy for phase segregation was calculated through equation 12：

$$k_{migration} = \frac{e^2 N v_0 d^2}{6\varepsilon_0 \varepsilon_{perovskite} k_B T} e^{\frac{\Delta S}{k_B}} e^{-\frac{\Delta H}{k_B T}} \quad (12)$$

where ΔS represents the changes in the entropy of a single ion migration step obtained from our calculation; k_B is the Boltzmann constant; ν_0 is the attempt frequency for an ion to hop which was extracted from Ni *et al.*'s work[59]; d is the ionic hopping distance, which depended on the lattice parameter of the unit cell; E_a is the activation energy, which is represented here by enthalpy (ΔH). ΔH was also obtained from our DFT calculation, e is the elementary charge, $\varepsilon_{perovskite}$ is the dielectric constant of the perovskite, ε_0 is the dielectric constant in a vacuum, and N is the doping density obtained from literature[34]. The previous study assumed that the migration rate was largely proportional to the activation energy for the phase

segregation because all the parameters except E_a (ΔH) could be regarded as constants in the discussed situation[33]. However, for our study, the doping density and the dielectric constant were changing with atmospheres and pressure under illumination. Hence, we deduced that the migration rate also changed. The activation energy was described as

$$-\ln\kappa_{migration} = -\ln\frac{e^2 v_0}{6\xi_0 k_B T} - \ln\frac{Nd^2}{\xi_{perovskite}} - \frac{\Delta S}{k_B} + \frac{\Delta H}{k_B T} \quad (13)$$

The various parameters entering equation (13) are given in Supplementary Table 13.

Transient absorption (TA) spectroscopy at low pressure. The femtosecond 400 nm pump and white-light probe were used as the illumination source for light soaking. The white light continuum generated by a non-collinear optical parametric amplifier consisted of a visible pulse light between 520 nm and 780 nm operated at a 1 kHz repetition rate, with an average power of ~400 μW. The white-light pulse was equally divided into probe and reference, before being focused onto the sample to an effective beam radius of ~100 μm, corresponding to energy per pulse of ~630 μJ·cm^{-2} for each split beam and a carrier density of ~10^{20} cm^{-3} at the perovskite film.

The sample film was loaded into a cube cell with spectroscopic windows on the front and back in a glove box. Before the optical measurements, the cell was connected to a vacuum pump (HiCube 80 Eco), being pumped overnight in the dark until the pressure stabilized at 3.4 × 10^{-3} Pa. The vacuum pump was kept working continuously during the measurement to ensure a stable pressure. The output of a Ti:sapphire amplifier system (Spectra-Physics Solstice Ace) operating at 1 kHz and generating ~100 fs pulses was split into the pump and probe beam paths. The visible broadband beam was generated in a home-built non-collinear optical parametric amplifier (NOPA), and the white light was split into two separate beams, one probe and one reference beam. The 400-nm pump beam was created by sending the 800-nm fundamental

beam of the Solstice Ace through a second harmonic generating (SHG) beta barium borate (BBO) crystal of 1 mm thickness (Eksma Optics). The pump was blocked by a chopper wheel rotating at 500 Hz while a computer-operated a mechanical delay stage to adjust the delay between the pump and the probe. The transmitted probe and reference pulses were collected by a silicon dual-line array detector (Hamamatsu S8381-1024Q), which was driven and read out by a custom-built board (Stresing Entwicklungsbüro).

'Drift-Diffusion' model for device performance simulation. We used SCAPS-1D (a Solar Cell Capacitance Simulator) to build the device model as the architecture shown in Fig 1a. Detailed parameters are illustrated in Table S5-S12 and extracted from the literature[60,61].

X-ray photoelectron spectroscopy. The chemical composition of films was measured using XPS (Kratos Ultra) with an Al Kα radiation source, and all the binding energies were calibrated by carbon as a reference.

Data availability

All data generated or analysed during this study are included in the published article and its Supplementary Information and Source Data files. The data can also be found at the following public repository: 10.14459/2021mp1620140.

Acknowledgments

Financial support from Deutsche Forschungsgemeinschaft (DFG, German Research Foundation) via Germany´s Excellence Strategy – EXC 2089/1 – 390776260 (e-conversion) and via International Research Training Group 2022 Alberta / Technical University of Munich

International Graduate School for Environmentally Responsible Functional Materials (ATUMS) as well as from TUM.solar in the context of the Bavarian Collaborative Research Project Solar Technologies Go Hybrid (SolTech) is acknowledged. L. D. thanks the Cambridge Trust and R. G., W. C., L. D., N. L., T. X., S. L. thank for the financial support from the Chinese Scholarship Council (CSC). S.P. acknowledges support from the TUM International Graduate School of Science and Engineering (IGSSE) via the GreenTech Initiative Interface Science for Photovoltaics (ISPV) of the EuroTech Universities, the excellence cluster Nanosystems Initiative Munich (NIM) and the Centre for NanoScience (CeNS).

*Corresponding author

muellerb@ph.tum.de

Author contributions

R.G.: conceptualization, methodology, formal analysis, investigation, resources, data curation, writing-original draft, project administration, visualization. D. H., and H. E.: investigation and formal analysis for density function calculation, writing – original draft. W.C.: resource and investigation for beamtime, supervision. L. D.: investigation and formal analysis for transient absorption spectra, writing – original draft.. K. W.: validation and resources for the project. K. J. and S. D. S.: resources and investigation for transient absorption spectra. Q. X. and P. G.: resources and investigation for X-ray photoelectron spectroscopy. S. L and M. Y: resources and investigation for Brunauer–Emmett–Teller measurement. L. K. R: software and resources. M. A. S., S. P, S. Y., N. L, T. X, and A.L.O: resources and investigation for the beamtime. S. L. and C. L.W.: visualization. N. C. G., and R, F.: investigation and formal analysis for transient absorption spectra. M. S, and S.V.R: resources, investigation, methodology and curation for the beamtime. P.M.B.: conceptualization, funding acquisition, project administration, validation. All authors contribute to writing-review & editing.

Competing interests

S. D. S. is a co-founder of Swift Solar. All other authors declare no competing interests.

Supplementary information

(SI file attached)

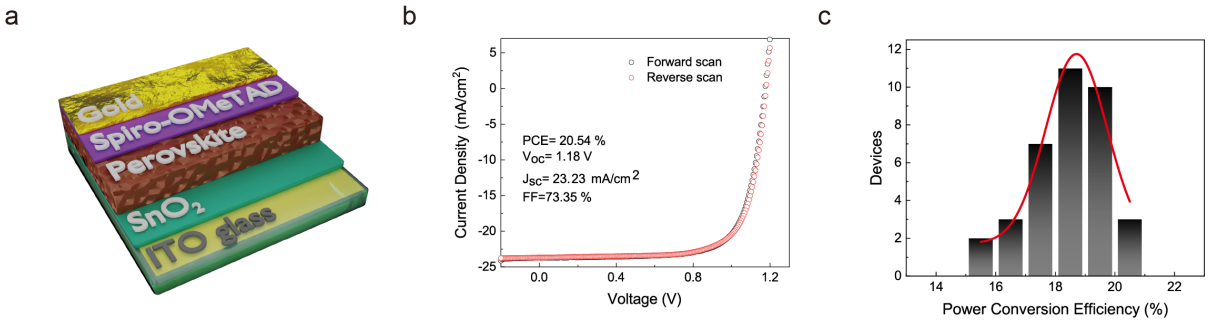

600

601

602 **Fig. 1. Structure and performance of the devices analysed.** (a) Sketch of the device
603 architecture of fabricated planar MAFA perovskite solar cells. (b) J-V scan of the champion
604 device for MAFA perovskite solar cells and related device parameters. (c) Histogram of PCE
605 obtained from 36 fabricated MAFA PSCs with red line displaying a Gaussian fit.

606

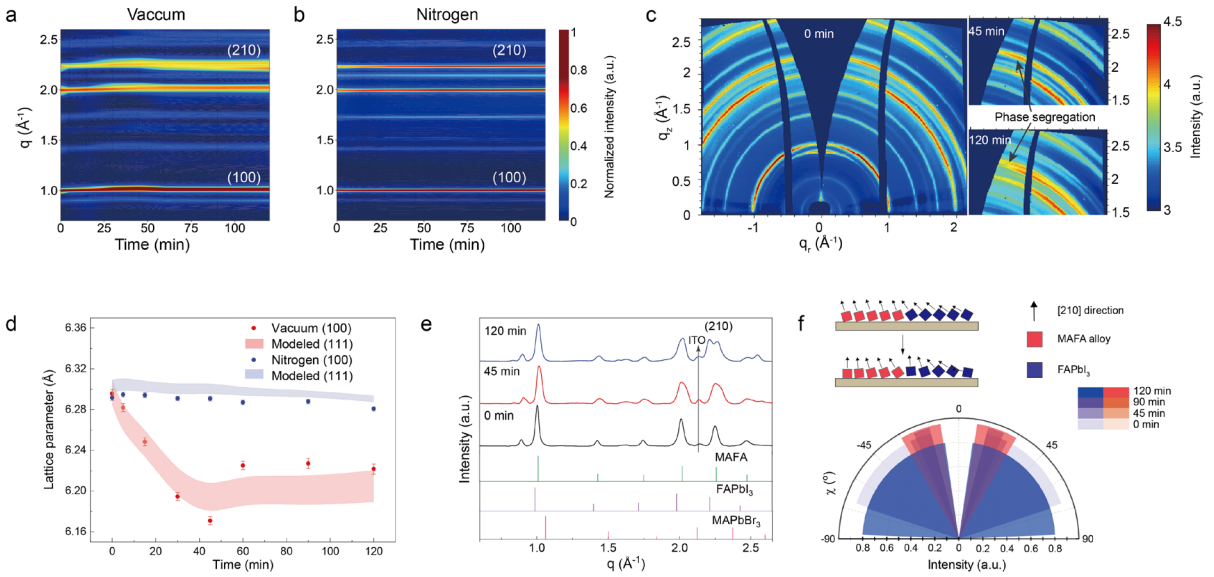

Fig. 2. Structure evolution of MAFA PSCs operating in different atmospheres. (a,b) Time-evolution of *operando* synchrotron radiation-based GIWAXS data plotted as azimuthally integrated line profiles of 2D GIWAXS data for the operation of MAFA PSCs under vacuum (a) and nitrogen (b) based on the ISOS-L-1I protocol. (c) Temporal evolution of 2D GIWAXS data transferred to q-space and collected under vacuum during the operation of the solar cell for 0, 45 and 120 minutes. (d) Lattice evolution for different atmospheres (vacuum in red, nitrogen in blue) as a function of illumination time. Filled circles denote the measurements with error bars derived from three-times fit through the Gaussian distribution of the (100) Bragg peak. The shaded areas display the modeled (111) peaks, reflecting a non-uniform shrinkage for all lattice directions. (e) Evolution of radial GIWAXS profiles integrated over all azimuthal angles (pseudo-XRD profiles) during operation for MAFA PSCs in vacuum, and simulated MAFA, $FAPbI_3$, and $MAPbBr_3$ perovskite XRD scattering patterns. (f) Crystallite orientation evolution during operation for MAFA perovskite under vacuum (stronger colour patterns indicate the orientation of crystals after longer operation times) reconstructed from the

623 tube cuts of the 2D GIWAXS data at the (210) Bragg peak. The schematic diagram shows the
624 evolution of the crystallite orientation.
625

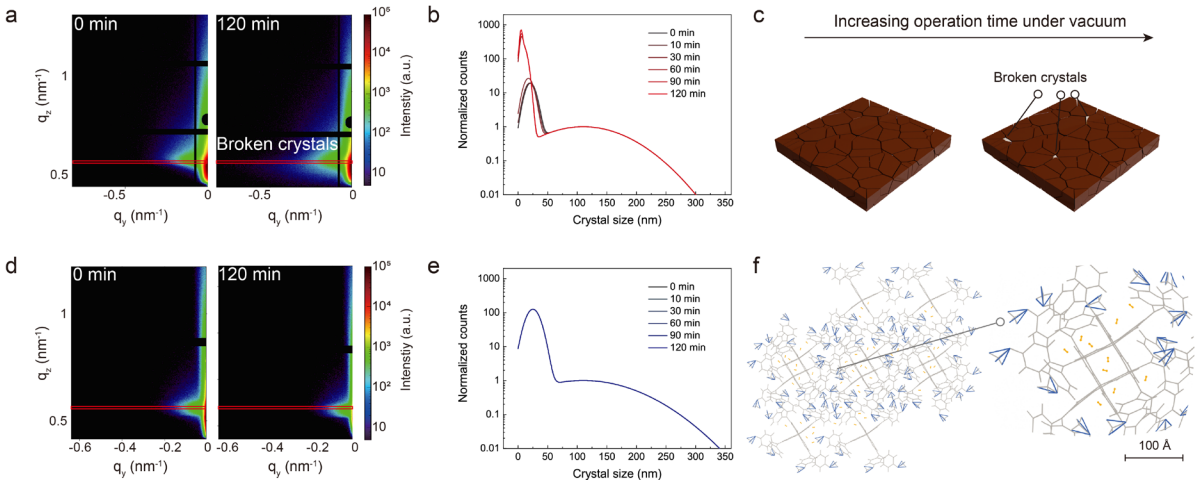

Fig. 3. Morphology evolution of MAFA PSCs operating in different atmospheres. (a) Time evolution of 2D GISAXS data under operation in vacuum (red line indicates the horizontal line cut at the perovskite Yoneda peak position). (b) Evolution of crystal size distributions under operation in vacuum for different form factors extracted from the model and intensity-normalized to form factor 1 (~110 nm). (c) Scheme to illustrate the improved strength of the perovskite film to suppress further deformation through the increase of grain boundaries due to broken crystals. (d) Time evolution of 2D GISAXS data under operation in a nitrogen atmosphere (red line indicates the horizontal cut at the perovskite Yoneda peak position). (e) Evolution of crystal size distributions under operation in a nitrogen atmosphere for different form factors extracted from the model and normalized to form factor 1 (~110 nm). (f) Schematic diagram of nitrogen molecules (yellow symbols) diffusing through the spiro-OMeTAD layer expressed by a blue (side chains) and grey (intermolecular π-π stackings) mixed space frame during the operation of solar cells under nitrogen. The zoomed inset indicates the loose structures of spiro-OMeTAD allowing the diffusion of nitrogen molecules.

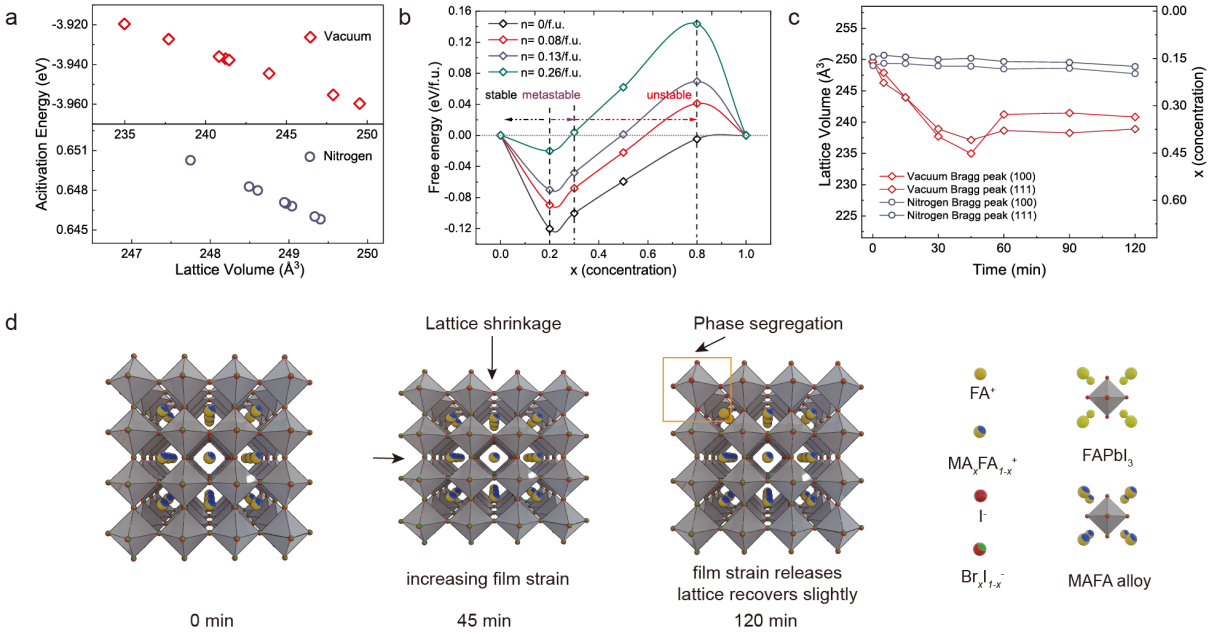

643

644

645 **Fig. 4. The thermodynamic driving force of lattice shrinkage and phase segregation.** (a)
646 Evolution of activation energies for phase segregation as a function of lattice volume under
647 vacuum (red) and a nitrogen atmosphere (blue). (b) Density-functional theory calculated
648 Helmholtz free energy ΔF^{*}_{mix} of $(MAPbBr_3)_x(FAPbI_3)_{1-x}$ (x=0, 0.2, 0.3, 0.5, 0.8 and 1) at room
649 temperature (T = 300 K) for different photo-excited charge carrier densities n. The black,
650 purple and red dash lines indicate the stable, metastable and unstable phase for different
651 compositions of the perovskite, respectively. (c) The lattice volume evolution translated to
652 related compositional ratios as a function of the operation time in different atmospheres. (d)
653 Schematic diagram projecting the non-uniform lattice shrinkage during the operation of PSCs
654 in vacuum, followed by the phase segregation of the MAFA perovskite, which is highlighted
655 by an orange frame.

656

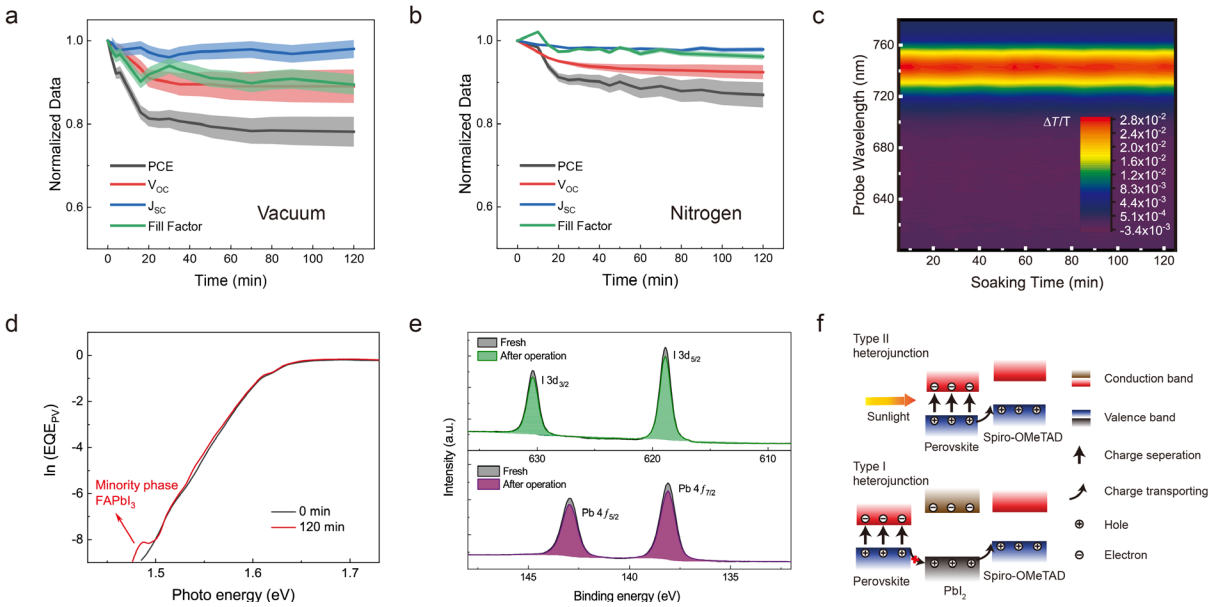

Fig. 5. Degradation Mechanisms of MAFA PSCs under the ISOS-L-1I protocol in different atmospheres. (a) Evolution of PCE (black), J_{SC} (blue), V_{OC} (red), and FF (green) measured by the reverse scan (from 1.3 V to -0.2 V) under vacuum. (b) Evolution of PCE, J_{SC}, V_{OC}, and FF measured by the reverse scan in nitrogen. For (a) and (b), the shaded areas indicate error bars extracted from the standard deviation of normalized PCE, J_{SC}, V_{OC} and FF values of 6 devices operated are operated under the ISOS-L-1 protocol in different atmospheres. (c) *In situ* transient absorption spectra (100 to 120 ps average) of the perovskite active layer as a function of illumination time under vacuum (3.4×10^{-3} Pa). The colour bar indicates the change in the transmission (absorption) of the broadband probe pulse when the sample is photoexcited by a pump pulse. (d) Photovoltaic external quantum efficiencies (EQE_{PV}) of $(MAPbBr_3)_{0.17}(FAPbI_3)_{0.83}$ PSCs measured before and after the operation in vacuum. (e) The change of XPS I3d and Pb4f spectra for $(MAPbBr_3)_{0.17}(FAPbI_3)_{0.83}$ PSCs measured before and after the operation under voltage-bias conditions, and the baseline of data is extracted through a Shirley background correction. (f) Schematic illustration for the effects of the migration of PbI_2 to the interface between perovskite and spiro-OMeTAD.

675 **References:**

676 1. Rong, Y. *et al.* Challenges for commercializing perovskite solar cells. *Science* **361**,
677 (2018).
678 2. Jeon, N. J. *et al.* Solvent engineering for high-performance inorganic–organic hybrid
679 perovskite solar cells. *Nature Materials* **13**, 897–903 (2014).
680 3. Jeon, N. J. *et al.* Compositional engineering of perovskite materials for high-performance
681 solar cells. *Nature* **517**, 476–480 (2015).
682 4. Yang, W. S. *et al.* Iodide management in formamidinium-lead-halide–based perovskite
683 layers for efficient solar cells. *Science* **356**, 1376 (2017).
684 5. Best Research-Cell Efficiencies.
685 6. Cardinaletti, I. *et al.* Organic and perovskite solar cells for space applications. *Solar*
686 *Energy Materials and Solar Cells* **182**, 121–127 (2018).
687 7. Tu, Y. *et al.* Mixed-cation perovskite solar cells in space. *Science China Physics,*
688 *Mechanics & Astronomy* **62**, 974221 (2019).
689 8. Reb, L. K. *et al.* Perovskite and Organic Solar Cells on a Rocket Flight. *Joule* **4**, 1880–
690 1892 (2020).
691 9. Deretzis, I. *et al.* Stability and Degradation in Hybrid Perovskites: Is the Glass Half-
692 Empty or Half-Full? *J. Phys. Chem. Lett.* **9**, 3000–3007 (2018).
693 10. Mahesh, S. *et al.* Revealing the origin of voltage loss in mixed-halide perovskite solar
694 cells. *Energy Environ. Sci.* **13**, 258–267 (2020).
695 11. Li, N. *et al.* Microscopic Degradation in Formamidinium-Cesium Lead Iodide Perovskite
696 Solar Cells under Operational Stressors. *Joule* **4**, 1743–1758 (2020).
697 12. Tsai, H. *et al.* Light-induced lattice expansion leads to high-efficiency perovskite solar
698 cells. *Science* **360**, 67 (2018).

13. Rolston, N. *et al.* Comment on 'Light-induced lattice expansion leads to high-efficiency perovskite solar cells'. *Science* **368**, eaay8691 (2020).
14. Domanski, K., Alharbi, E. A., Hagfeldt, A., Grätzel, M. & Tress, W. Systematic investigation of the impact of operation conditions on the degradation behaviour of perovskite solar cells. *Nature Energy* **3**, 61–67 (2018).
15. Khenkin, M. V. *et al.* Consensus statement for stability assessment and reporting for perovskite photovoltaics based on ISOS procedures. *Nature Energy* **5**, 35–49 (2020).
16. Zhou, Q. *et al.* High-Performance Perovskite Solar Cells with Enhanced Environmental Stability Based on a (p-FC6H4C2H4NH3)2[PbI4] Capping Layer. *Advanced Energy Materials* **9**, 1802595 (2019).
17. Bi, D. *et al.* Efficient luminescent solar cells based on tailored mixed-cation perovskites. *Sci Adv* **2**, e1501170 (2016).
18. Jesper Jacobsson, T. *et al.* Exploration of the compositional space for mixed lead halogen perovskites for high efficiency solar cells. *Energy Environ. Sci.* **9**, 1706–1724 (2016).
19. Zhang, Y. *et al.* Trash into Treasure: δ-FAPbI3 Polymorph Stabilized MAPbI3 Perovskite with Power Conversion Efficiency beyond 21%. *Advanced Materials* **30**, 1707143 (2018).
20. Jiang, Q. *et al.* Planar-Structure Perovskite Solar Cells with Efficiency beyond 21%. *Advanced Materials* **29**, 1703852 (2017).
21. Roose, B., Dey, K., Chiang, Y.-H., Friend, R. H. & Stranks, S. D. Critical Assessment of the Use of Excess Lead Iodide in Lead Halide Perovskite Solar Cells. *J. Phys. Chem. Lett.* **11**, 6505–6512 (2020).
22. Beal, R. E. *et al.* Structural Origins of Light-Induced Phase Segregation in Organic-Inorganic Halide Perovskite Photovoltaic Materials. *Matter* **2**, 207–219 (2020).

723 23. Hoke, E. T. *et al.* Reversible photo-induced trap formation in mixed-halide hybrid
724 perovskites for photovoltaics. *Chem. Sci.* **6**, 613–617 (2015).
725 24. Chapter 9 - Epilogue. in *Pergamon Materials Series* (eds. Banerjee, S. & Mukhopadhyay,
726 P.) vol. 12 783–800 (Pergamon, 2007).
727 25. Gleiter, H. Chapter 9 - MICROSTRUCTURE. in *Physical Metallurgy (Fourth Edition)*
728 (eds. Cahn, R. W. & Haasen†, P.) 843–942 (North-Holland, 1996). doi:10.1016/B978-
729 044489875-3/50014-4.
730 26. Lu, K., Lu, L. & Suresh, S. Strengthening Materials by Engineering Coherent Internal
731 Boundaries at the Nanoscale. *Science* **324**, 349 (2009).
732 27. Jariwala, S. *et al.* Local Crystal Misorientation Influences Non-radiative Recombination
733 in Halide Perovskites. *Joule* **3**, 3048–3060 (2019).
734 28. Lin, Y.-H. *et al.* A piperidinium salt stabilizes efficient metal-halide perovskite solar
735 cells. *Science* **369**, 96 (2020).
736 29. Agnew, S. R. 2 - Deformation mechanisms of magnesium alloys. in *Advances in Wrought*
737 *Magnesium Alloys* (eds. Bettles, C. & Barnett, M.) 63–104 (Woodhead Publishing, 2012).
738 doi:10.1533/9780857093844.1.63.
739 30. Eperon, G. E. *et al.* The Role of Dimethylammonium in Bandgap Modulation for Stable
740 Halide Perovskites. *ACS Energy Lett.* **5**, 1856–1864 (2020).
741 31. Brunauer, S., Deming, L. S., Deming, W. E. & Teller, E. On a Theory of the van der
742 Waals Adsorption of Gases. *J. Am. Chem. Soc.* **62**, 1723–1732 (1940).
743 32. Hutter, E. M. *et al.* Thermodynamic Stabilization of Mixed-Halide Perovskites against
744 Phase Segregation. *Cell Reports Physical Science* **1**, 100120 (2020).
745 33. Muscarella, L. A. *et al.* Lattice Compression Increases the Activation Barrier for Phase
746 Segregation in Mixed-Halide Perovskites. *ACS Energy Lett.* **5**, 3152–3158 (2020).

747 34. Hu, Z. *et al.* The Impact of Atmosphere on Energetics of Lead Halide Perovskites.
748 *Advanced Energy Materials* **10**, 2000908 (2020).
749 35. Juarez-Perez, E. J. *et al.* Photoinduced Giant Dielectric Constant in Lead Halide
750 Perovskite Solar Cells. *J. Phys. Chem. Lett.* **5**, 2390–2394 (2014).
751 36. Ahmadi, M. *et al.* Environmental Gating and Galvanic Effects in Single Crystals of
752 Organic–Inorganic Halide Perovskites. *ACS Appl. Mater. Interfaces* **11**, 14722–14733
753 (2019).
754 37. Wang, X. *et al.* Suppressed phase separation of mixed-halide perovskites confined in
755 endotaxial matrices. *Nature Communications* **10**, 695 (2019).
756 38. Erkey, C. Chapter 4 - Thermodynamics and Dynamics of Adsorption of Metal
757 Complexes on Surfaces from Supercritical Solutions. in *Supercritical Fluid Science and*
758 *Technology* (ed. Erkey, C.) vol. 1 41–77 (Elsevier, 2011).
759 39. Alberti, A. *et al.* Nitrogen Soaking Promotes Lattice Recovery in Polycrystalline Hybrid
760 Perovskites. *Advanced Energy Materials* **9**, 1803450 (2019).
761 40. Correa Baena, J. P. *et al.* Highly efficient planar perovskite solar cells through band
762 alignment engineering. *Energy Environ. Sci.* **8**, 2928–2934 (2015).
763 41. Jiang, Y. *et al.* Mitigation of Vacuum and Illumination-Induced Degradation in
764 Perovskite Solar Cells by Structure Engineering. *Joule* **4**, 1087–1103 (2020).
765 42. Burgelman, M., Nollet, P. & Degrave, S. Modelling polycrystalline semiconductor solar
766 cells. *Thin Solid Films* **361–362**, 527–532 (2000).
767 43. Jeangros, Q. *et al.* In Situ TEM Analysis of Organic–Inorganic Metal-Halide Perovskite
768 Solar Cells under Electrical Bias. *Nano Lett.* **16**, 7013–7018 (2016).
769 44. Kaienburg, P. *et al.* How Contact Layers Control Shunting Losses from Pinholes in Thin-
770 Film Solar Cells. *J. Phys. Chem. C* **122**, 27263–27272 (2018).

45. Jiang, Q. *et al.* Enhanced electron extraction using SnO2 for high-efficiency planar-structure HC(NH2)2PbI3-based perovskite solar cells. *Nature Energy* **2**, 16177 (2016).
46. Saliba, M. *et al.* How to Make over 20% Efficient Perovskite Solar Cells in Regular (n–i–p) and Inverted (p–i–n) Architectures. *Chem. Mater.* **30**, 4193–4201 (2018).
47. Buffet, A. *et al.* P03, the microfocus and nanofocus X-ray scattering (MiNaXS) beamline of the PETRA III storage ring: the microfocus endstation. *J Synchrotron Radiat* **19**, 647–653 (2012).
48. Chen, W. *et al.* Operando structure degradation study of PbS quantum dot solar cells. *Energy Environ. Sci.* **14**, 3420–3429 (2021).
49. Gunthard, B., Wolfgang, wagermaier, Chenghao, L., Stephan, V. R. & Peter, F. A customizable software for fast reduction and analysis of large X-ray scattering data sets: applications of the new DPDAK package to small-angle X-ray scattering and grazing-incidence small-angle X-ray scattering. *Journal of Applied Crystallography* **47**, 1797–1803 (2014).
50. Jiang, Z. GIXSGUI: a MATLAB toolbox for grazing-incidence X-ray scattering data visualization and reduction, and indexing of buried three-dimensional periodic nanostructured films. *Journal of Applied Crystallography* **48**, 917–926.
51. Xie, L.-Q. *et al.* Understanding the Cubic Phase Stabilization and Crystallization Kinetics in Mixed Cations and Halides Perovskite Single Crystals. *J. Am. Chem. Soc.* **139**, 3320–3323 (2017).
52. Draguta, S. *et al.* Rationalizing the light-induced phase separation of mixed halide organic–inorganic perovskites. *Nature communications* **8**, 1–8 (2017).
53. Clerc, D. G. & Cleary, D. A. Spinodal Decomposition as an Interesting Example of the Application of Several Thermodynamic Principles. *J. Chem. Educ.* **72**, 112 (1995).

54. Kresse, G. & Furthmüller, J. Efficient iterative schemes for ab initio total-energy calculations using a plane-wave basis set. *Phys. Rev. B* **54**, 11169–11186 (1996).
55. Perdew, J. P. *et al.* Restoring the Density-Gradient Expansion for Exchange in Solids and Surfaces. *Phys. Rev. Lett.* **100**, 136406 (2008).
56. Umari, P., Mosconi, E. & De Angelis, F. Relativistic GW calculations on CH3NH3PbI3 and CH3NH3SnI3 Perovskites for Solar Cell Applications. *Scientific Reports* **4**, 4467 (2014).
57. Brivio, F., Butler, K. T., Walsh, A. & van Schilfgaarde, M. Relativistic quasiparticle self-consistent electronic structure of hybrid halide perovskite photovoltaic absorbers. *Phys. Rev. B* **89**, 155204 (2014).
58. Thind, A. S., Huang, X., Sun, J. & Mishra, R. First-Principles Prediction of a Stable Hexagonal Phase of CH3NH3PbI3. *Chem. Mater.* **29**, 6003–6011 (2017).
59. Ni, Z. *et al.* Resolving spatial and energetic distributions of trap states in metal halide perovskite solar cells. *Science* **367**, 1352 (2020).
60. Calado, P. *et al.* Evidence for ion migration in hybrid perovskite solar cells with minimal hysteresis. *Nature Communications* **7**, 13831 (2016).
61. Miyata, A. *et al.* Direct measurement of the exciton binding energy and effective masses for charge carriers in organic–inorganic tri-halide perovskites. *Nature Physics* **11**, 582–587 (2015).